Soft Matter

PAPER

View Article Online
View Journal | View Issue

Cite this: *Soft Matter*, 2025, **21**, 5468

Capillary-induced adhesive contact dynamics determines dissipation and flow structure in wetted hydrogel packings

Zohreh Farmani, [ab] Jing Wang, [c] Ralf Stannarius [c] and Joshua A. Dijksman [*ab]

The bulk response of a granular material is strongly influenced by particle and contact properties, such as friction coefficients, particle softness, lubrication on the contact scale and adhesion between particles. This study explores the bulk flow of wetted hydrogel particles, which are soft but also weakly adhesive due to capillary bridges. This simplified granular material with minimal contact friction reveals key insights in the role of capillary stresses on the macroscopic flow. At the micro-scale, we demonstrate a direct correlation between relative humidity (RH) and liquid bridge size between two wetted hydrogel spheres, with an average rupture distance increasing with humidity. On the macro scale, the wetted hydrogel sphere packings show remarkable flow dissipation and flow behavior in the split-bottom shear cell. We retrieve flow fields of the hydrogel packing with magnetic resonance imaging and measure flow resistance with a rheometric technique. The shear bands for the adhesive hydrogels are much narrower than for dry grain flows. The change in flow resistance due to a change in filling height can be interpreted with a minimization argument, indicating that the flow dissipation is set entirely by the capillary bridge stress: the capillary stress at all filling heights dominates the gravitational stress. We confirm this view by exposing the flowing packing to an external pressure. Beyond a confining stress of 250 Pa, the shear bands become significantly thinner, approaching some plateau at 360 Pa. This underscores the importance of understanding micro-scale interactions in controlling macroscopic hydrogel particle packing behavior.

Received 3rd March 2025,
Accepted 29th May 2025

DOI: 10.1039/d5sm00221d

rsc.li/soft-matter-journal

1 Introduction

Anyone who has ever built a sand castle knows that one needs a bit of water to turn loose sand grains into a good building material. This everyday experience is representative of the general fact that the bulk properties of particulate materials or so-called "bulk solids" are strongly influenced by particle interactions, even if they are very weak. Specifically, in the case of sticky, slightly wet grains, it remains important to comprehend how particle–particle interactions in the presence of liquids affect the intricate mechanics and physics of wet particulate materials.[1,2] When wet particles come into contact with each other or with a solid surface, their contact behavior differs significantly from that of dry particles. This disparity arises primarily from the formation of a liquid bridge between wet particles, which introduces distinctive bulk flow characteristics compared to dry systems.[3–7] One effect that plays a role is that frictional forces on particle contacts can become substantially larger due to the presence of the normal forces induced by the capillary effects, for example providing the ability to build a sand castle with vertical walls. Liquid bridges form due to contact adhesion or attractive forces arising between (partially deformable) particles upon contact. Various types of liquid bridges, including pendular (low liquid content), funicular (medium liquid content),[8] and capillary (high liquid content, particles are completely encapsulated with liquid), have been characterized.[9] Liquid bridges also play a vital role in the behavior of particles under compression or indentation,[10–12] as they contribute to the particle resistance to deformation by establishing adhesive forces between constituent particles.[13] Understanding the mechanisms of contact adhesion provides insights into micro-scale particle behavior[14–16] and aids in the design of materials with tailored mechanical properties. The presence of liquid bridges has been shown to significantly influence particle flow, transforming particle behavior from individual grains to clumps.[17,18]

[a] *van der Waals-Zeeman Institute, Institute of Physics, University of Amsterdam, Science Park 904, 1098 XH Amsterdam, The Netherlands. E-mail: j.a.dijksman@uva.nl*
[b] *Physical Chemistry and Soft Matter, Wageningen University & Research, Stippeneng 4, 6708 WE Wageningen, The Netherlands*
[c] *Institute of Physics, Otto von Guericke University Magdeburg, Universitätsplatz 2, D-39106 Magdeburg, Germany*

Hydrogel particle packings are distinct from regular particle packings as a result of various differences between the hydrogel material and the typically stiffer materials of which most other granular ensembles are made. Another major difference is that hydrogel–hydrogel contacts have a very low friction coefficient. The actual friction coefficient depends on the hydrogel used, the sliding rate, the normal force and likely other chemical factors.[19] The maximum ratio of normal to tangential forces that a hydrogel–hydrogel contact can sustain is typically estimated to be smaller than 0.01. As there are no frictional forces to activate, how do capillary effects change the flow behavior of such low-friction particle packings? The investigation of weakly hydrated (''wetted'') soft particle mixtures is particularly interesting, as the formation of capillary bridges can exert pressures that compete with other stress scales in soft, low-friction particle systems, such as lubrication forces and deformation. How does contact adhesion affect flow and microstructure? To what extent can we quantify the effect of adhesion in soft adhesive grain packing? How is the bulk flow behavior affected by capillary contacts?

We show here that millimeter-sized hydrogel particle packings are strongly affected by capillary necks. Despite the weakness of capillary bridges with respect to gravitational forces, as evidenced by our direct contact measurements, wetted hydrogel particle packings show distinct flow features that sets them apart from their submersed equivalent. Our magnetic resonance imaging (MRI)-based measurements indicate that the quasi-static flow behavior of the packing displays very narrow shear bands and a strong dependence on the flow geometry, suggesting that capillary interactions can generate strong dissipation at the contact level. Further confined flow measurements and rheometer-based dissipation measurements support the unconfined flow geometry-based interpretation in terms of capillary-induced dissipation, providing at once a novel method to probe the role of contact adhesion on the stresses and flow behavior in a slowly flowing granular material. Finally, rate dependent measurements of wetted hydrogel packings reveal a rate dependence that suggests that capillary forces can activate a rate-dependent dissipation mechanism between the hydrogel particles.

2 Liquid bridge mechanics

We first probe the contact mechanics of a capillary neck between two hydrogel particles, to quantitatively establish the adhesive forces on a single hydrogel–hydrogel contact. These contact force measurements are not as trivial as in static, rigid spheres, as hydrogel spheres can absorb water from their bulk into the capillary neck, making the traditional capillary contact models less useful, as they rely on constant liquid bridge volumes.[20] Moreover, the hydrogel spheres have relaxation mechanics of their own,[21] and an unknown but likely finite contact angle[22] that we call θ, all of which may affect capillary neck mechanics. We therefore first explore the contact dynamics of two wet hydrogel spheres separately. We expose the two spheres in contact to various RH environments and contact timescales as they are likely to encounter in the packing of sheared particles.

2.1 Setup for capillary adhesion measurements

The setup is depicted in Fig. 1. We secured two equally sized hydrogel spheres with 10 mm diameter in holders that covered approximately two-thirds of the spheres. The top holder was connected to a 50 g capacity load cell. We also aligned the particles in the x and y direction. The bottom particle remained fixed to the lab frame, while the top particle was brought into contact with the second sphere and then retracted. During the entire contact process (approach and retraction), we measured the force and displacement. We approached the first particle towards the second particle at a constant velocity v_a, then allowing for a relaxation period (contact time t_c) to ensure particle equilibration. This (probably poroelastic) relaxation time allows for the particles to adjust, redistributing forces and potentially accommodating changes in shape or inter-molecular forces

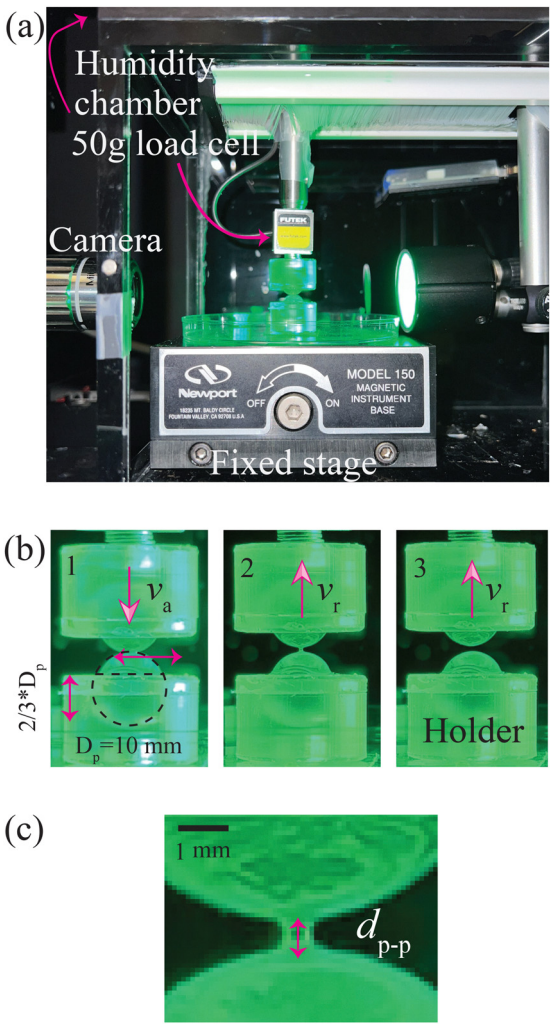

Fig. 1 (a) Indentation setup placed inside a closed humidity chamber. (b) Two particles with D_p = 10 mm are held in place by 3D-printed holders. (1) Top particle approaches with the speed of v_a to the bottom one. (2) Top particle retracts with the speed of v_r. (3) The particles are completely separated. The holder covers two third of the particle. (c) Zoom into part b2: during retraction, a liquid bridge forms between the particles. The key parameter extracted from the liquid bridge is the rupture distance d_{p-p}.

within the particle gel network before measurements during separation. Moreover, during the relaxation period t_c, stress redistribution might occur within the particles. In the next step, the first particle was retracted from contact at a velocity v_r. All measurements were performed within a chamber in which the relative humidity was controlled. The process was monitored using a camera, allowing us to quantify the properties of the liquid bridge formed between the particles.

We systematically varied the relative humidity (RH) and adjusted the contact time t_c to study relaxation effects. The approach velocity v_a and retraction velocity v_r were varied to examine the influence of contact (lubrication) dynamics on the magnitude of the inter-particle forces. Additionally, we explored the effect of contact force F_M variation on the deformation and rupture distance between the particles.

Fig. 2 illustrates the formation of a liquid bridge during the retraction of the top particle from the bottom one, captured at relative humidities of 20% (Fig. 2a), 40% (Fig. 2b), 60% (Fig. 2c), and 80% (Fig. 2d). We observe changes in the shape, rupture distance, and volume of the liquid bridge as relative humidity increases. We note that the contact angle does not show significant dependence on the RH. From theory,[22] we expect a finite contact angle: even though the hydrogel material is superabsorbent and hence likely charged and thus prefers to be surrounded by bulk water, the outer polymer strands on the surface of the sphere will at least partially adsorb on the water–air interface, creating an energy penalty for the wetting of hydrogel surface, leading to finite contact angle. The variation in particle–particle distance throughout the frames is shown in Fig. 3, which is extracted from a single recording of the approaching and retracting particles.

To analyze the liquid bridge properties, we processed the recorded videos from experiments. The images were converted to grayscale to simplify the processing, and a thresholding technique was applied to segment the dark spheres from the background, resulting in a binarized image. To detect the boundaries of the spheres and calculate the change in distance as they interact, two red circle segments were fitted to the sphere surfaces (Fig. 3a). We calculated the distance between the boundaries of the spheres along the vertical axis (assuming the spheres are aligned vertically). Typical results are shown in (Fig. 3b).

The rupture distance for contacting spheres refers to the separation or retraction distance between their surfaces before rupture. We observed that the rupture distance increases with increasing relative humidity RH due to the increased amount of liquid within the bridge (Fig. 4).

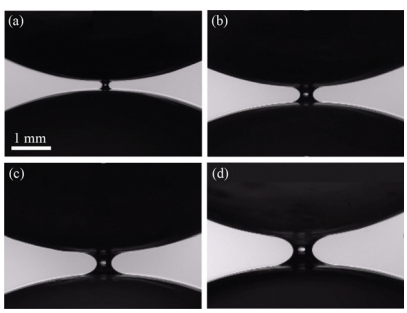

Fig. 2 Liquid bridge captured from particle–particle dynamics just before break-off at (a) RH 20%, (b) 40%, (c) 60%, and (d) 80%.

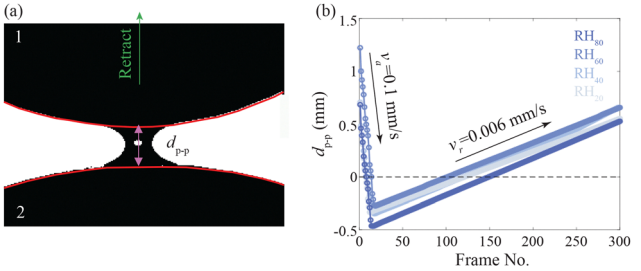

Fig. 3 Particle–particle distance at constant contact force F_M of 10 mN and constant approach speed v_a of 0.1 mm s^{-1} and constant retraction speed v_r of 0.006 mm s^{-1}, (a) two red circular arcs are fitted to the boundaries of the spheres for tracking displacement. We calculate the maximum distance between two spheres before rupturing and we denote that to the rupture distance, (b) tracking arcs provides particle–particle distance as a function of time at different RH = 20%, 40%, 60%, and 80%. The constant approach and retraction velocities (v_a,v_r) are indicated by arrows.

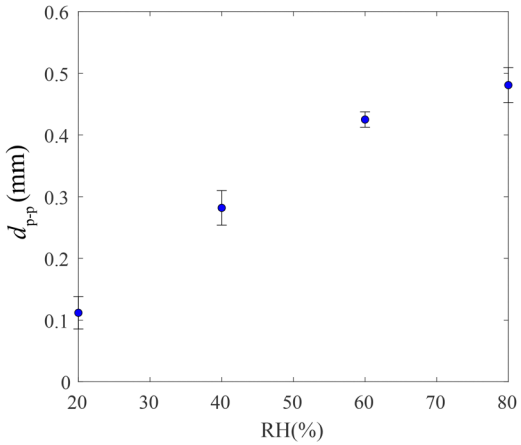

Fig. 4 Rupture distance d_{p-p} as a function of RH = 20, 40, 60, 80%. The error bars represent the standard deviation of triplicate measurements.

Furthermore, when two particles approach and then retract from each other, we measure the force–displacement relationship (Fig. 5). We call the total amount of displacement of the top sphere d. The starting point is always at a finite distance $d > 0$ from the bottom sphere. Initially, as they approach (red line), the two spheres are separated, and the force is zero. When the top sphere moves downward and touches the bottom sphere, there is a sudden increase in the force, primarily due to the Hertzian elastic response. After the contact point (at $d \approx 1$ mm for most experiments), we observe a slight negative force up to $d \approx 1.2$ mm, which is followed by a sharp increase in the force until it reaches the maximum contact force or overlap. The small negative dip is a result of a liquid bridge forming.

2.2 Adhesive force dynamics

The experimentally measured force response is the difference between the Hertzian elastic response of the spheres in contact

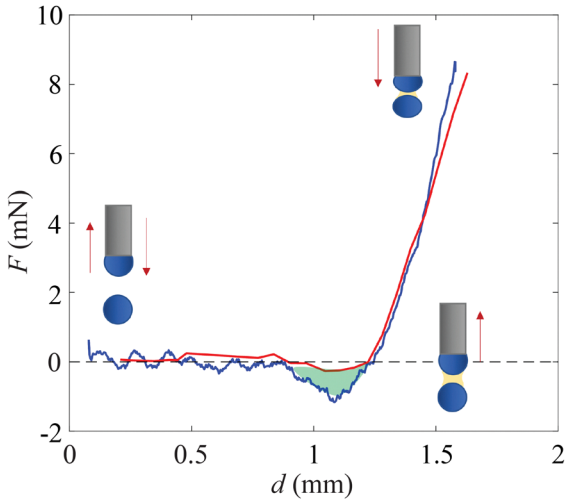

Fig. 5 Force–displacement plot at contact force F_M = 10 mN, relative humidity RH = 80%, t_c = 1 s and retraction speed v_r = 0.006 mm s^{-1}. The approach curve is represented by ▬, and retraction curve by ▬. The green part represents the area under the F–d plot and hence the total dissipation in the loss of contact. Here, d means the distance by which the upper sphere is lowered respective to the initial position.

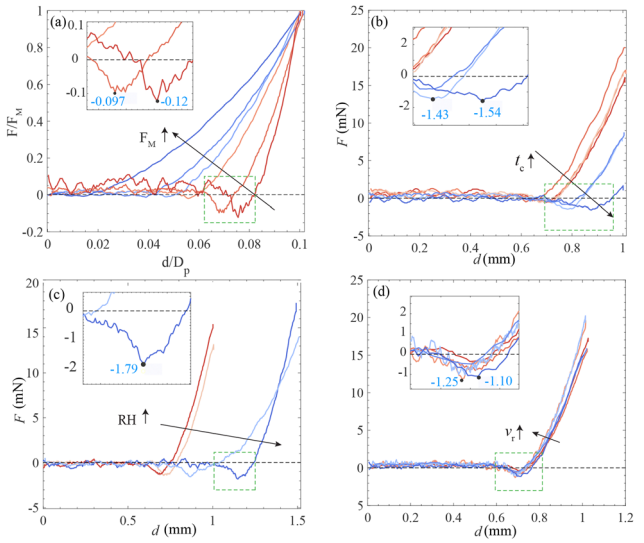

Fig. 6 Force–displacement plots at different (a) contact force F_M = 1 ▬, 7 ▬, 10 ▬, 20 ▬, 30 ▬, 50 ▬, 80 mN ▬, constant RH = 40%, t_c = 1 s and v_r = 0.006 mm s^{-1}, (b) contact time t_c = 1 ▬, 10 ▬, 50 ▬, 100 ▬, 500 ▬, 1000 ▬, 2000 s ▬, constant F_M = 10 mN, and v_r = 0.008 mm s^{-1}, (c) relative humidity RH = 20% ▬, 40% ▬, 60% ▬, 80% ▬, constant F_M = 10 mN, t_c = 1 s and v_r = 0.006 mm s^{-1}, and (d) retraction speed v_r = 0.008 ▬, 0.006 ▬, 0.003 ▬, 0.001 ▬, 0.05 ▬, 0.01 mm s^{-1} ▬, constant F_M = 10 mN, t_c = 1 s, and RH = 40%. Insets show close ups of the green dashed-line boxes.

(when there is a contact) and the emerged capillary neck, which establishes itself upon contact and exists until its rupture at finite separation distance. Crucially, we do not know how much liquid the neck extracts out of the sphere: some water may be getting sucked from the sphere due to capillary stresses or imbibed from elsewhere on the surface of the hydrogel sphere. We can hence not disentangle these contributions. The deformation of the sphere, combined with the change in neck volume as the spheres approach, makes it challenging to extract the separate magnitude of these two contributions; such a study would require a separate work. We can, however, establish the capillary adhesive contact force dynamics experimentally.

2.2.1 Maximum adhesive force. During retraction (blue line), the top sphere moves back up at some point, leading to a decrease in the force. In the retraction phase, there is a pronounced dip (green region) where a certain negative force is reached, with $F_{adh} \approx 1.8$ mN. This dip represents the maximum force required to pull the two spheres apart (pull-off or adhesive force), indicating only the adhesive contribution due to the formation of the liquid bridge, which due to the prolonged and enhanced indentation grew larger than originally formed at the contact moment. We can also uniquely attribute the negative forces in the retraction phase to capillary effects, as elastic contributions must be entirely absent beyond a point where the spheres lose contact. In the final step, with further retraction, the liquid bridge ruptures (at $d \approx 1$ mm in this example) and the two spheres separate, returning the force to zero.

2.2.2 Adhesion parameters. We also reproduced the F–d retraction plots for different parameters such as maximum contact force F_M (Fig. 6a), contact time t_c (Fig. 6b), relative humidity RH (Fig. 6c), and retraction speed v_r (Fig. 6d). By changing all these parameters we do not observe any significant effect on the adhesion peak force. However, there are some changes in the force–distance plots in the case of increasing maximum contact force (F_M). We plotted the normalized force (F/F_M) *versus* the normalized distance (d/D_p) to enable a clearer comparison across different contact forces (Fig. 6a). As a result, the curves at lower contact forces now exhibit a clear dip near ≈ -0.12 (-0.12×10 mN $= -1.2$ mN), corresponding to the reported adhesion force range of -1.1 to -1.8 mN. At higher contact forces, the dip becomes less pronounced due to material softening and distributed detachment effects, which is consistent with the viscoelastic and deformable nature of the hydrogel particles. By changing contact time t_c from 1 to 2000 s, the F–d plots shift to the right along with a decrease in the maximum contact force and an large pull-off force. The rightward shift in the F–d plot signifies delayed compression, potentially more gradual stress redistribution, decreased maximum force, and increased energy dissipation due to the longer contact time between the particles and the viscoelastic response of the hydrogel matrix. The decrease in the maximum contact force suggests that despite the extended contact duration, the maximum force experienced during the interaction is lower. This could imply that the particles can equilibrate better, redistribute stresses and reduce the force observed. The third parameter studied is the RH. Increasing RH from 20 to 80% results in a rightward shift in the F–d plot. The rightward shift indicates that higher relative humidity can prolong the time it takes for the spheres to separate during retraction, causing the compression phase to extend over a longer distance, due to larger liquid bridge volumes. Moisture content so causes the spheres to adhere more and take longer to separate. Finally, the last parameter v_r appears to have no

significant impact on the F–d plot within the observed range (from 0.001 to 0.008 mm s^{-1}). Soft particles may have a characteristic response time, and changes in retraction speed within certain limits might not affect the compression or separation dynamics enough to be visible in the plot.

2.2.3 Adhesive force interpretation. In our experiment, we observed a maximum capillary-driven adhesive force of $F_{adh} \approx 1.8$ mN in all studied cases. Although observed close to pinch off, this value is not far from the predicted $F_c = 2\pi R\gamma \cos\theta$ based on capillary neck theory. Here, R is the radius of the spheres used in the adhesion tests and γ is the surface tension of the contact liquid, all as specified in Table 1. We gain two insights from this experimental result. First of all, based on the assumption that this force scale is also relevant during elastic (wetted) loading of the contact, Hertz elasticity theory for a sphere yields a maximum Hertz contact pressure p_0 of about 2000 Pa. This results comes from the textbook[23] relation

$$p_0 = \left(\frac{6F_c E_p^{\,2}}{\pi^3 R^2}\right)^{1/3}, \quad (1)$$

in which E_p is the modulus of the hydrogel particle. We note that in a round Hertzian contact between a sphere and another surface, there is a radially symmetric stress profile, that is decreasing quadratically from its peak value p_0 in the center, reaching zero at the edge of said surface. The average contact stress is hence much lower than 2000 Pa.

Second, we can relate the adhesive contact forces to another relevant force scale, namely gravity. The granular Bond number[24–27] under gravity is then a helpful concept, which contrasts the maximum attractive force during contact with a single grain's weight.

$$\mathrm{Bo_g} = \frac{F_c}{W} = \frac{2\pi R\gamma\cos(\theta)}{mg} = \frac{6\gamma\cos(\theta)}{4R^2\rho g} \quad (2)$$

where again F_c is the (maximum) capillary force, W is weight of the particle, m is the mass of the particle, and g is the gravitational acceleration. We so estimate the dimensionless granular Bond to be of the order of 0.4. This indicates that the weight of a single sphere is comparable to the maximum attractive force due to adhesion. In an unconfined flow, capillary adhesion can thus already play a significant role.

Table 1 Particle properties and parameters used in the experiments

Particle properties	Settings
Diameter 1 (flow tests) (D_{p1})	2–3 mm
Diameter 2 (adhesion tests) (D_{p2})	10 mm
Density (ρ)	999 kg m^{-3}
Particle Young's modulus (E_p)	10 kPa
Particles Poisson's ratio (ν_p)	0.5
Water density (ρ_f)	997 kg m^{-3}
Rotation rate (ω_0)	0.02 rad s^{-1}
Rotation angle (θ)	10°
Strain steps (N)	7
Split disk radius (mm)	47.5
Outer fixed plate radius (mm)	75
Maximum allowed filling height (mm)	100

3 Flow structure of dense, wetted hydrogel sphere packings

3.1 Split-bottom shear cell, MRI experiments

In the context of bulk shear flows, in the so-called split-bottom shear cell (SBSC), extensive studies have examined how various particle and contact properties—such as friction, softness, and adhesion affect the compression of sheared granular materials.[6,18,27–31] We use the magnetic resonance imaging (MRI) technique to obtain high-resolution structural and dynamical information of hydrogel packings in the SBSC. Detailed information on the MRI measurement method can be found elsewhere.[32] Our focus is on studying the shearing behavior of soft adhesive hydrogels in an SBSC, as this geometry produces well-developed shear bands away from the boundaries of the shear cell.[33,34] The hydrogels used here were 2–3 mm in diameter, initially swelled in water and subsequently wetted. Experimental parameters are also provided in Table 1, and the design of the SBSC used in this study can be found elsewhere.[35] At the beginning of experiments, our SBSC was filled with a material layer of depth H, and then driven, stepwise, in each step with a constant rotation of an inner bottom disk with a radius of R_s = 47.5 mm. A schematic sketch of the SBSC is shown in Fig. 7. Within the MRI scanner, we performed experiments under two types of applied pressure: (1) shear under constant hydro-static particle pressure (P_{hyd}), which means the flow structure was not confined by a lid, and (2) shear while varying constant confining pressures P from the top boundary, which we refer to as the "confined flow structure". We provide the results of these different experimental conditions in the two following subsections. In each measurement, step-wise shear with a constant rate of ω_0 was applied. We performed the experiments in step-wise

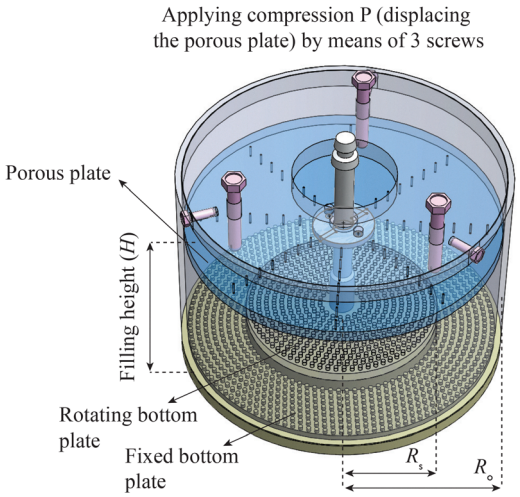

Fig. 7 Schematic of the split-bottom shear cell (SBSC) with two rough bottom plates, an inner rotating plate called split disk with radius R_s = 47.5 mm, and an outer fixed plate with radius R_0 = 75 mm. The maximum fill height allowed by the geometry is H = 100 mm. There is a movable, porous top plate and a fixed top plate attached to three screws by which we impose a certain confining pressure P on the packing. By turning the screws we displace the porous plate and compact the packing.

mode to allow for imaging after each strain step. In the first set of experiments, the unconfined case, the filling height H and thus the ratio of height to inner disk radius (H/R_s) was varied as a tuning parameter to control the exerted pressure P_{hyd} on the packing. In the second set of experiments, the confined case, an additional pressure source was introduced for every H/R_s through a porous plate placed on top of the packing; the top plate could be positioned at different fixed heights to control the volume of the particle packing. We calibrated the stress exerted separately using a rheometer, where the normal force F_N was recorded by displacing the plate in 2 mm increments for a packing with an initial height of 50 mm.

To determine the angular velocity fields in a cross section of the SBSC, we employed particle image velocimetry (PIV) of the 3D MRI images. To create smooth PIV fields with high resolution, we assumed axial symmetry of the displacement field. In this approximation, we can obtain the absolute displacement of hydrogel material in the "square donut" space given by a small range in both vertical coordinate h and radial coordinate r, *via* an image intensity cross-correlation approach. This displacement was calibrated with the simultaneously measured rotation angle of the bottom disk and served as the angular velocity $\omega(h,r)$, relative to the rotation rate ω_0 of the bottom disk. The data were averaged over 5 strain steps for each H/R_s. We verified that an initial transient was only two strain steps long, it was removed from the analysis. With this approach, we determined the displacement of particles at a given (h,r) from the MRI image stacks.

3.2 Unconfined flow structure

We first probe the flow behavior of unconfined packings, in which only gravity provides the confining stress. Fig. 8a shows a two-dimensional (2D) displacement of particles at a given (h,r) for different filling heights H extracted by PIV from MRI 3D tomograms. In the shallow layers (H = 15 mm), a narrow and nearly vertical shear band is formed between the moving zone above the rotating disk and the static zone. As we increase the filling height and move towards the deeper layers, we observe collapsing of the shear band from vertical to horizontal. There are three distinguishable regions though, (1) a trumpet-like structure in shallow layers (H/R_s = 0.31, 0.42), (2) an intermediate region showing a mixture of trumpet and dome structures (H/R_s = 0.5, 0.59), and (3) a dome-like structure in deep layers (H/R_s = 0.65, 0.95, 1.05). At approximately H/R_s = 0.59 the shear band still reaches the top surface. However, by increasing the fill height by another 3 mm, the particles at the surface become static and a dome with the thickness of few particle layers appears on top of the rotating disk. At $H \approx R_s$, we observe a completely closed dome. The phenomenology of the flow fields is very similar to that of dry granular flows and suspensions in the SBSC,[36] yet a close look at the flow profiles reveals one essential difference.

By taking a cross-section from 2D profiles of Fig. 8a at a constant $h = H/2$, we look at the non-dimensional angular velocity profile $\omega(r)/\omega_0$, defined as the ratio of the time-averaged azimuthal velocity to the driving rate ω_0, with a high radial

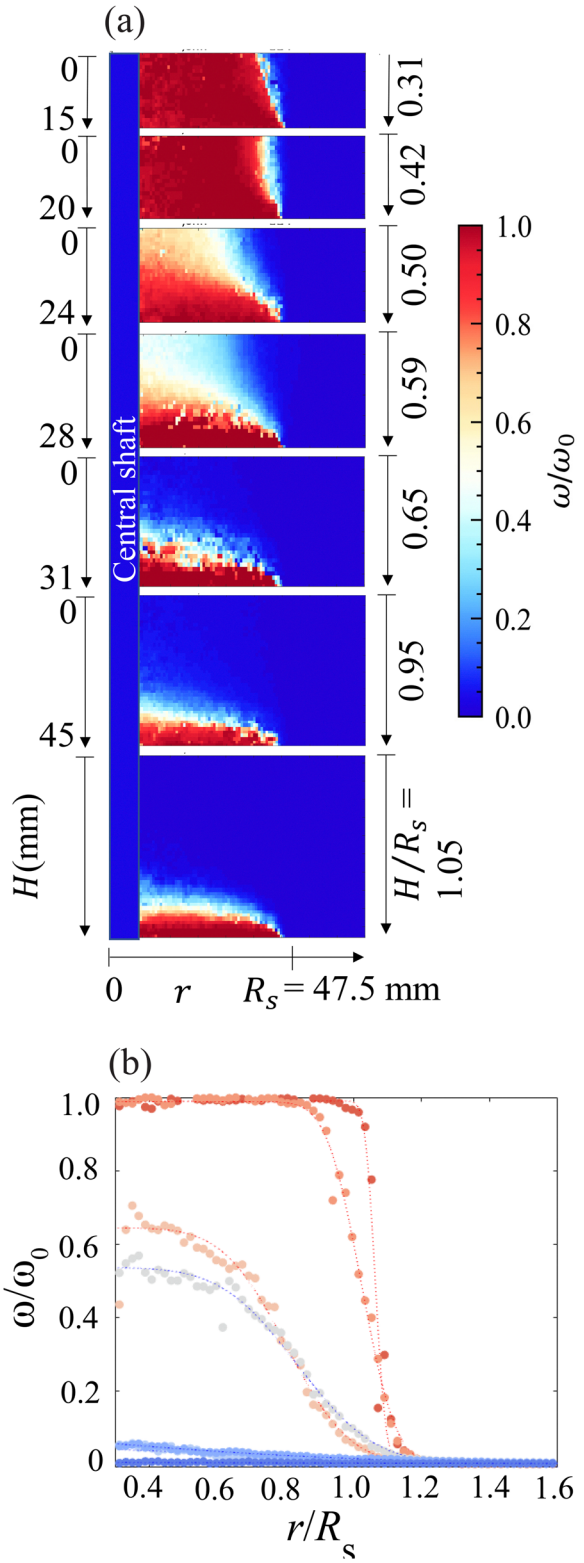

Fig. 8 (a) 2D unconfined flow profiles at a given (h,r) extracted from PIV, for adhesive hydrogel packing, in beds of different heights from H = 15 mm to H = 50 mm. (b) Normalized averaged angular velocity profiles for a range of filling heights H = 15 mm ●, 20 mm ●, 24 mm ●, 28 mm ●, 31 mm ●, 45 mm ●, and 50 mm ●. The graph shows the relative rotation speed at height H along a ring of radius r for adhesive hydrogels. For all runs, R_s is 47.5 mm. All the profiles are fitted with an error function (dotted lines), see eqn (3). The slight scatter of the data is due to experimental uncertainty and indicates the typical error on ω.

resolution obtained by PIV (Fig. 8b). As usual, we can observe a general trend in the $\omega(r)/\omega_0$ curves with the three distinguishable regions of shallow, intermediate, and deep layers. From $H/R_s = 0.31$ (15 mm) to $H/R_s = 1.05$ (50 mm), the slope of the curves representing the shear bands decreases and the shear band moves inward from totally vertical to horizontal. All profiles fit well with an error function equation established in previous studies:[32,34]

$$\omega(r) = \frac{A\omega_0}{2}\left[\mathrm{erf}\left(\frac{R_c - r}{\delta}\right) + 1\right], \quad (3)$$

where R_c is the location of the shear band center, δ is the shear bandwidth, and ω_0 is the rotational speed of the bottom disk. A is a fit parameter used for those profiles whose plateau at small r cannot be observed or is smaller than one due to the overall shape of the shear profile, for example, in the case of dome flow. However, for the shallow layers, the shear bands are surprisingly narrow: for the lowest filling height, the shear bands are about half a particle diameter wide, contrary to the typical wide shear zones that are observed in the SBSC filled with hard grains. Even for $H/R_s = 1.05$, we find that $\delta \approx 4D_p$.

3.2.1 Shear band shape analysis. It seems appropriate to assume that the local stress that determines the local frictional behavior is now not just determined by gravity. The adhesive forces of the capillary bridges are significant, as per the Bond number estimates. The capillary forces so make the particles stick together and move as a adhesive solid mass, with only very little ability to create a smoothly flowing transition zone between the two boundaries of the SBSC, one of which is moving, and one of which is static. The capillary forces induce contact stresses, deformation and liquid bridge rearrangements, all of which add to the dissipative mechanisms during the flow.

If dissipative mechanisms only play a role in the very narrow shear zones, we can use the torque minimization argument from Unger *et al.*[37] to estimate the transition from vertical to dome-shaped shear bands. The hydrostatic pressure gradient is not an important stress scale in this system, as the gravitational stress $\simeq \rho gH$ for a 1 cm layer of wetted hydrogels is about 100 Pa. As eqn (1) showed, the maximum contact stress due to capillarity can exceed that significantly. We find that for the 10 mm diameter hydrogel particles of the microscopic study, the peak Hertz theory contact stress was approximately 2000 Pa; for the smaller spheres used in the flow study, this peak stress increases to >2 kPa as per the scaling in eqn (1). As we also know that the flow is quasistatic and the particles polydisperse[38,39] (hence crystallization is unlikely) we can assume that the shear stresses are predominantly set by capillary stresses, which are essentially uniform throughout the packing. The total amount of dissipation is then proportional to the surface area between the static and moving bulk.

To estimate the surface area of the shear zone, we can see that at low fill heights, if the shear zone is perfectly vertical, it resembles a cylinder and the surface area depends linearly on H/R_s (shown as the solid black line in Fig. 9a). At intermediate filling heights, the shear zone collapses and we should

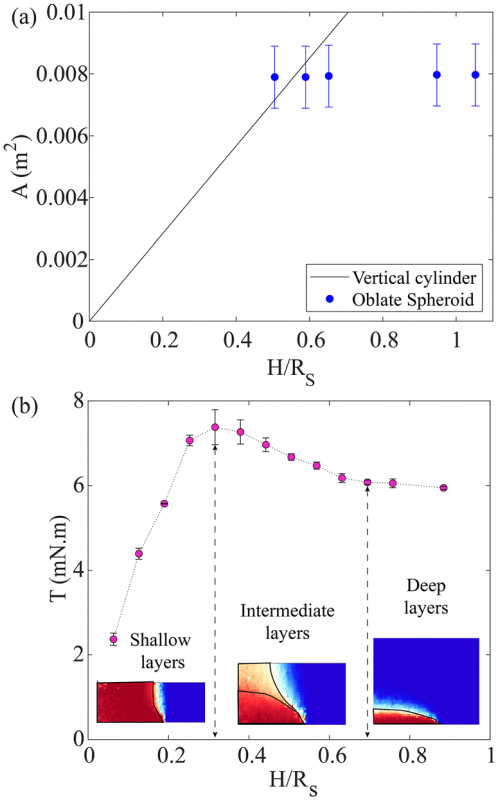

Fig. 9 (a) Calculated shear zone surface area as a function of filling height H/R_s for both a vertical cylinder at R_s (solid line) and half of an oblate spheroid with a height experimentally estimated where $\omega(z) = \omega_0/2$ as observed for the shear zones at different H/R_s. The error bars indicate the effect of the shear zone height estimate at $r = 0$. (b) Torque as a function of filling height. Three flow regimes can be observed: shallow layers, intermediate layers and deep layers. The error bars represent the standard deviation of triplicate measurements.

approximate the shape of the shear zone as an oblate half-spheroid. With the MRI data at hand, we can estimate the height $z = z_P$ of the oblate half-spheroids observed for larger filling heights, by estimating where the normalized angular velocity $\omega(z = z_P) = 1/2$. We can then compute the sliding surface areas in the filling height regimes discussed by using the standard equation for the surface S of a paraboloid:[40]

$$S = 2\pi R_s^2\left(1 + \frac{z_P^2 \tanh^{-1}(e)}{eR_s^2}\right) \quad (4)$$

Here, $e = \sqrt{1 - (z_P/R_s)^2}$. The results with estimates for $z_P(H/R_s)$ are shown in Fig. 9a. When H/R_s increases, we observe the dome shaped shear zone precisely at the filling height where a cylinder with said filling height would have exceeded the shear surface of the actually observed dome shapes shear band: at approximately 24 mm filling height, a nearly spheroidal shear zone becomes smaller than the cylinder surface area, triggering a system transition. We conclude that the system aims to minimize the shear zone area, influenced by friction coefficient considerations.[37,41] We can gain additional

evidence for this mechanical picture by measuring the dissipated power as a function of filling height.

3.2.2 $T(H)$ dependence: measuring dissipation. We measured the dissipation during flow *via* the torque T as we increased the filling height H keeping a constant rotation rate of $\omega_0 = 0.02$ rad s^{-1}. As we shall see below, the weakly adhesive particles do not appear to have a rate-independent regime, so essentially any slow rotation rate suffices for this reference measurement because we are only interested in the effect of H. Fig. 9 shows three distinguishable regions of the flow that we observed in the 2D profiles of Fig. 8. In shallow layers where the shear band is vertical, we see a linear increase in the torque as we increase the filling height to $H = 15$ mm. In the intermediate region between $H = 18$ to 33 mm the torque suddenly drops from $\approx$7.5 to 6 mN m. By moving to the deep layers, the torque reaches a plateau at the three last filling heights. This behavior of the torque is different from what one can observe for completely dry or completely submersed particle packings.[42] In suspensions or dry packings, at small H, the torque increases quadratically with the filling height due to the combined effect of hydro-static pressure, height increase and flow profile change. In the wetted adhesive hydrogel system, a (height independent) adhesive force controls the normal force of contacts and hence the dissipation between the particles. The initial linear increase in $T(H)$ can thus be considered a consequence of an increasing surface of the trumpet on which in every point the same shear stress is acting. For intermediate layers, the trumpet shape changes into a dome flow, reducing surface area, leading to a lower T. For even larger H, the dome shape is constant while the stresses are always dominated by the (constant) adhesive properties of the spheres, leading to a plateau in T in the deep layer regime. In this scenario, the packing height becomes irrelevant as the contact stress scale is primarily determined by adhesion. In contrast, for dry or submersed systems, the constant dome shape at these filling heights is under increasing pressure as H increases, leading to $T \propto H$. The specific $T(H)$-behavior of adhesive powders in the SBSC can be a useful general tool to characterize the adhesive properties of bulk solids, complementing other methods such as the FT4 and Schulze tester.[43]

3.2.3 Water distribution in a wetted hydrogel packing. One aspect to address in wetted hydrogel packings is the somewhat non-uniform distribution of liquid throughout the packing. We visually observe higher amount of liquids in the pores at the bottom of the packing than on the surface. We can therefore not assume a perfectly constant average adhesive stress as a function of depth. To assess the magnitude of the deviation, we used X-ray micro-tomography (GE Phoenix microtome) to scan a small packing of hydrogel spheres as used in the MRI/SBSC experiments. The resulting 3D images (Fig. 10) reveal a densely packed configuration with substantial water content within the pores. This observation suggests that the packing resides in the capillary state of the liquid bridge, wherein all particles are surrounded by water. However, the imaged packing is static and does reveal substantial pores within the structure itself, which due to their surface tension can significantly affect the mechanics of the particles. Moreover, these voids are affected by shear, and on average may still provide substantial adhesive effects. Estimating the average adhesive stress due to these pores and capillary necking in the capillary or funicular bridges is a challenging problem. Many-body effects[44] likely also play a role in these flowing packings. We note also that the X-ray scan was performed in a small cuvette and therefore may have suffered from large boundary effects.

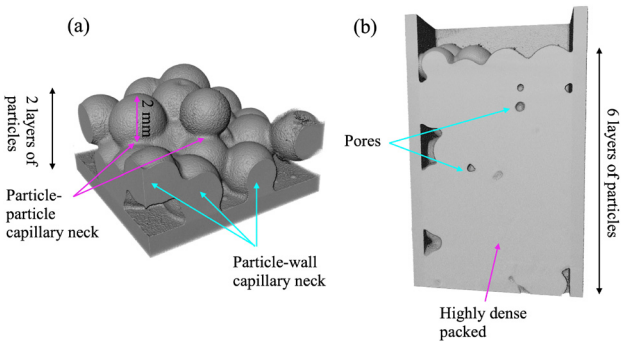

Fig. 10 3D rendered images of $\approx$ 2 mm hydrogel spheres obtained from X-ray micro-tomography. (a) Side view without the surrounding wall, showing two layers of spheres filled in a couette cell. The change in sphere shape at contact points with each other and the wall allows visualization of the locations of liquid bridges. Additionally, (b) side view with the surrounding wall, showing multiple layers of spheres, revealing a highly dense packed bed with few pores. It indicates the presence of liquid bridges in a capillary state where particles are completely encapsulated with water with limited pore spaces.

3.3 Confined flow structure

We can get an indication that the nonuniform distribution of pore fluids has a limited effect on the capillary effects by performing flow studies of the hydrogels under confinement of a lid with fixed position. In our confined flow study, we performed a combined set of experiments: step-wise shear experiments followed by a step-wise compression. During the compression steps, we increased the confinement stress on the packing by moving down a porous plate on top of the hydrogel packing. At every compression step, we performed MRI measurements to probe the 3D flow structure and the total compression. We measured the displacement of particles at a given (h,r) using the MRI-PIV methods described above for every compression level P, to be clarified below. We performed a set of MRI measurements of confined packings, at initially constant filling heights of $H = 50$, 31, and 20 mm. We focus here on the results from the $H = 50$ mm case, noting that for this case, the fixed compression plate least affects the flow boundary condition at the top, as the surface velocity at this H/R_s is already very small even in the unconfined case. The results for other filling heights are qualitatively consistent. As before, we performed shear over 7 strain steps of 10° at $\omega_0 \approx 0.02$ rad s^{-1}. At $P = 0$, we observed the shear band in confined to the bulk and forms a dome-shaped structure, as in the unconfined case. By moving down the plate by fixed amounts using the set screws and increasing P, and then performing step-wise shear, the dome becomes flatter, and flow is ever more confined to the rotating plate (Fig. 11).

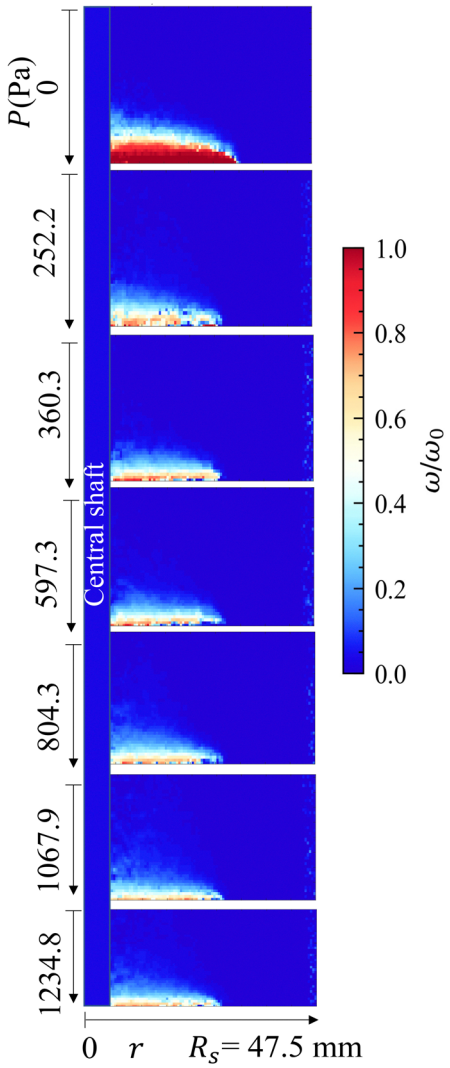

Fig. 11 2D flow profiles at a given (h,r) extracted from PIV, for confined flow at different pressure levels at initial filling height H = 50 mm. The blue bar indicates the position of the central shaft. Colors represent the normalized angular velocity ω/ω_0.

3.3.1 Calibrating the confining stress. To measure the pressure values corresponding to the movement of the confining plate, we conducted separate experiments. In these experiments, we attached a porous plate to the rheometer shaft and used the displacement control of the shaft and motor to apply a compression (loading) followed by releasing the compression (unloading) protocol on a wetted hydrogel packing. Concretely, we measured how the normal force and hence the pressure on the plate changes as we increase the compressive strain on the material (shown in the inset of Fig. 12). We started with the plate in a position where it does not touch the particle packing, to zero the normal force on the sensor. When we increased the strain to $\varepsilon = 0.07$, we observed a noticeable uptick in the force, due to the rearrangement of particles within the material. As we applied more strain, the pressure increased non-linearly, consistent with earlier observations.[45] At the maximum strain applied in the calibration experiment, the packing fraction has to increase from its loose initial state of approximately 63% of random close packing for frictionless spheres in three dimensions to a final volume fraction of approximately 85%, assuming that the hydrogel spheres do not change volume upon being compressed to this stress. Upon unloading, the hydrogel does not follow the same stress–strain curve as during loading. This difference between loading and unloading behavior, known as hysteresis, is a characteristic of compression tests on deformable hydrogels and indicates that the hydrogel dissipates some energy and potentially plastically deforms that we discuss elsewhere.[46] However, these loading–unloading cycles reproduce well, as can be seen in Fig. 12, and allow us to assign a compressive stress P to every MRI-PIV flow field at a given compressive strain, using the loading path as a lookup table for the confinement stress for every experiment. The results can be seen in Fig. 11.

The experimental results of compressed packing have two major consequences: (1) our results suggest that compression above $\approx$ 360 Pa does not observably change the shape of the profile; the shear band is confined to a shallow layer just above the disk. This indicates that we have reached a plateau region where further increases in confining pressure no longer probe any stress sensitivity in the packing. This limit is interesting as it allows us to probe the effect of confining stress on the packing itself. We also note that (2) during compression, the packing gets submersed into essentially all pore fluid available. The flowing material beyond a stress level of $\approx$ 250 Pa can be considered a submersed suspension.

3.3.2 $T(\omega)$ dependence: flow curve. In order to understand the flow dissipation of the wetted hydrogel packings in more detail, we recorded the torque T while conducting a rate ramp (10^{-4}–10^{1} rad s^{-1}). Fig. 13 shows an increase in torque when we increase the pressure. This indicates a very weak power-law trend with exponent of about 0.1 across all compression levels. Noticeably, at higher pressures, all contacts are subject to significant pressure owing to capillary bridges. We would like

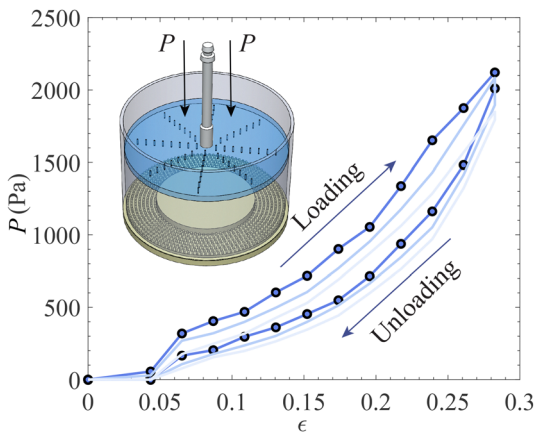

Fig. 12 Loading and unloading stress P of the adhesive hydrogel packing as a function of compressive strain ε. These experiments were conducted to determine the applied pressure to the packing when a specific strain is imposed. Three curves show three repeats of the same measurement. The first experiment is depicted as ●.

to highlight that the power law behavior in the rheology of even the unconfined wet hydrogel particles bears striking resemblance with that of the strongly compressed but submerged hydrogel packings we considered elsewhere.[35] In our view, the power law rheology emerges when the hydrogel particles are dominated by large adhesive or compressive contact stresses, triggering a dissipative contact evolution mechanism. Either capillary bridges or confinement are substantial enough (contact) pressure sources to make this contact level effect dominate the rheology of the packing. Our rheological data also indicate, that our quasi-static MRI experiments are not driven in a rate-independent regime, as such a regime does not appear to exist within the parameter range explored here. However, with the power-law exponent being low, we expect little influence of the said rate dependence within the minutes of scan time of the MRI tomograms.

4 Discussion

4.1 Micro-scale findings

4.1.1 Adhesive forces and liquid bridge formation. When two wetted hydrogel spheres come into contact, they experience an initial force increase due to elastic deformation. Upon retraction, a negative force is observed. This adhesive force is attributed to the formation of a liquid bridge that lasts until the bridge no longer has enough volume to span the separation between the separating surfaces. During this retraction, there is a pronounced dip in the force–displacement curve, indicating the maximum adhesive force required to separate the two spheres, representing the adhesive contribution due to the liquid bridge formation. The quantitative measurement of adhesion forces allowed us to establish that the Bond number of the adhesive packings used is low, and that the maximum contact stress is about 750 Pa.

4.1.2 Influence of relative humidity (RH). We observed a clear correlation between RH and the size of liquid bridges formed between the hydrogel spheres. At low RH (20%), the average rupture distance was approximately 0.5 mm, while at high RH (80%), the rupture distance increased to about 1.2 mm for the 10 mm sphere used. For smaller spheres, the breakup distance should be proportionally smaller, but the bridge length can thus be up to 10% of the diameter of the particle. As RH increases, the hydrogel affinity for retaining moisture and forming liquid bridges is enhanced; the bridge volume simply increases.[25] To assess the strength of capillary effects, we must consider that inside a (sheared) packing, the pore space is most likely always fully saturated with water. We can therefore assume that in the MRI flow experiments of our study, the hydration effects on the capillary bridge were constant and maximal.

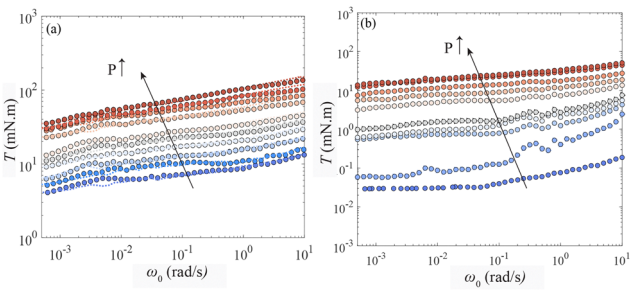

Fig. 13 The average driving torque T as a function of the driving rate ω_0 at constant filling height of H = 50 mm and different confined pressure P in (a) adhesive hydrogels, P = 0 Pa ●, 252.2 Pa ●, 360.3 Pa ●, 597.3 Pa ○, 804.3 Pa ○, 1067.9 Pa ○, 1234.8 Pa ○, 1332.7 Pa ●, 1538.6 Pa ●, 1652.7 Pa ●, and in (b) hydrogel suspension P = 0 Pa ●, 19.5 Pa ●, 80.4 Pa ●, 81.5 Pa ○, 93.5 Pa ○, 137.5 Pa ○, 240.7 Pa ○, 402.7 Pa ●, 696.7 Pa ●, and 880 Pa ●. The circles correspond to the forward rate ramp, while the dotted lines depict the backward curves. Both arrows indicate an increasing trend in the applied confining pressure P.

4.2 Macro-scale findings

4.2.1 Unconfined flow structure. In the unconfined flow structure, the behavior of the adhesive hydrogel particles in the SBSC was strongly influenced by the filling height (H). We observed a linear increase in torque as H increased up to 15 mm, suggesting a well-developed narrow shear band of constant shape in the shallow layers. In the intermediate region (H between 18 mm and 33 mm), a drop in torque occurred. This shift in behavior is associated with changes in the flow structure, and demonstrates the influence of the filling height on the macro-scale flow characteristics. Our MRI measurements support this picture. A quantitative estimate of the total surface area of the shear band shows that for adhesive hydrogel packings, a torque minimization principle also sets the position of the shear zone. The distinct thinning of the shear band in the presence of adhesion is not easily explained. Note that due to the profound difference of $T(H)$ for adhesive *versus* non-adhesive packings, a characterization of $T(H)$ for such grains in a split-bottom shear cell stands out as a potential tool for assessing the adhesive properties of powders or particles.

4.2.2 Confinement and pressure sensitivity. We also probed whether an external stress affects the flow behavior and flow dissipation of the wetted hydrogel packing. We applied an external pressure to the adhesive hydrogel packing and measured both flow dissipation and flow profiles. The results revealed that after reaching a pressure of approximately 250 Pa, the observed shear bands became even thinner than they already are due to adhesion in unconfined packings. Further increases in pressure, up to about 360 Pa, or about a quarter of the peak contact stress from Hertz theory as provided above, had minimal effect on the shear band's shape. This plateau region suggests that at a certain pressure threshold, the wetted hydrogel contact behavior becomes less sensitive to additional stress. We suspect two mechanisms to play a role: the non-linear nature of surface area increases in the Hertzian contacts, or the visibly more complete hydration of the packings under increased confinement. Hydration increases under compression, because the pore space is also reduced at elevated confinement stress: the packing of particles is substantially weaker than the 10 kPa hardness of the individual particles and hence it loses significant pore space even at only hundreds of Pa of confining stress. The data indicate that the capillary forces and particle–particle interactions are dominant factors in controlling the flow behavior in this confined macro-scale system.

5 Conclusion

We conducted microscale and macroscale experiments to investigate the behavior of wetted hydrogel particle packings. Adhesion measurements of the hydrogel particles revealed the systematic presence of capillary bridges under a wide range of loading speeds, maximum forces and contact durations and relative humidity conditions, and allowed to quantify a capillary contact stress scale of about 2 kPa, and establishing the magnitude of the Bond number in our packings. Our study sheds light on the complex interactions between hydrogel particles in which dynamics is set by capillarity, hydrogel swelling and elastic hydrogel properties. Using magnetic resonance imaging (MRI), we investigated the flow structure of hydrogel sphere packings in the SBSC setup. We varied the filling height and pressure applied to the packing, comparing confining pressures to contact pressure scales. We observed the formation of a narrow shear band in the unconfined, yet an even narrower one in the confined flow structure. The filling height had a significant impact on the shape of these bands, yet can be explained with a dissipation minimization principle, similar to such effects in non-adhesive dry particle flows in said geometry. The flow dissipation displayed a non-monotonic filling height effect that can also be rationalized from a shear surface minimalization perspective and may be used for characterization of particle adhesiveness. Our findings provide valuable insights into the flow behavior of adhesive (soft) particle packings and in particular hydrogel materials, offering a foundation for further research and the development of applications in *e.g.* adhesive powder mixtures and biomaterials.

Data availability

Data for this article is available at Zenodo repository with DOI: **https://doi.org/10.5281/zenodo.14945583**.

Conflicts of interest

There are no conflicts to declare.

Acknowledgements

This project has received funding from the European Union's Horizon 2020 research and innovation programme under the Marie Skłodowska-Curie grant agreement CALIPER no 812638. We acknowledge insightful discussions with Frans Leermakers. Cindy Lübeck and Oliver Speck are acknowledged for making the MRI experiments possible.

Notes and references

1 T. Li, W. Meng, Y. Wang, A. Valia, R. Jamsandekar, R. Kumar, F. J. Muzzio and B. J. Glasser, *Part. Sci. Technol.*, 2022, **40**, 141–150.
2 P. Liu, C. Q. LaMarche, K. M. Kellogg, S. Leadley and C. M. Hrenya, *AIChE J.*, 2016, **62**, 3529–3537.
3 B. Buck, Y. Tang, N. G. Deen, J. Kuipers and S. Heinrich, *Chem. Eng. Res. Des.*, 2018, **135**, 21–29.
4 H. Shi, R. Mohanty, S. Chakravarty, R. Cabiscol, M. Morgeneyer, H. Zetzener, J. Y. Ooi, A. Kwade, S. Luding and V. Magnanimo, *KONA Powder Part. J.*, 2018, **35**, 226–250.
5 S. Mandal, M. Nicolas and O. Pouliquen, *Phys. Rev. X*, 2021, **11**, 021017.
6 S. Roy, S. Luding and T. Weinhart, *New J. Phys.*, 2017, **19**, 043014.
7 A. Gans, B. Dalloz-Dubrujeaud, M. Nicolas and P. Aussillous, *Phys. Rev. Lett.*, 2024, **133**, 238201.
8 J.-P. Wang, E. Gallo, B. François, F. Gabrieli and P. Lambert, *Powder Technol.*, 2017, **305**, 89–98.
9 M. E. D. Urso, C. J. Lawrence and M. J. Adams, *J. Colloid Interface Sci.*, 1999, **220**, 42–56.
10 Y. Song and R. Turton, *Powder Technol.*, 2007, **178**, 99–108.
11 A. Hassanpour and M. Ghadiri, *Part. Part. Syst. Charact.*, 2007, **24**, 117–123.
12 J. Paul, S. Romeis, J. Tomas and W. Peukert, *Adv. Powder Technol.*, 2014, **25**, 136–153.
13 S. Luding, *Granular Matter*, 2008, **10**, 235–246.
14 C. Thornton, *A DEM study. Particle Technology Series*, 2015, vol. 24, pp. 21–47.
15 P. G. Rognon, J.-N. Roux, M. Naaim and F. Chevoir, *J. Fluid Mech.*, 2008, **596**, 21–47.
16 N. Mitarai and F. Nori, *Adv. Phys.*, 2006, **55**, 1–45.
17 E. L. Chan and K. Washino, *Chem. Eng. Res. Des.*, 2018, **132**, 1060–1069.
18 S. Roy, S. Luding and T. Weinhart, *Procedia Eng.*, 2015, **102**, 1531–1538.
19 M. Workamp and J. A. Dijksman, *J. Rheol.*, 2019, **63**, 275–283.
20 Y. I. Rabinovich, M. S. Esayanur and B. M. Moudgil, *Langmuir*, 2005, **21**, 10992–10997.
21 C. Shakya, J. van der Gucht and J. A. Dijksman, *Front. Phys.*, 2024, **12**, 1334325.
22 M. Cohen Stuart, W. De Vos and F. Leermakers, *Langmuir*, 2006, **22**, 1722–1728.
23 V. L. Popov *et al.*, *Contact mechanics and friction*, Springer, 2010.
24 S. T. Nase, W. L. Vargas, A. A. Abatan and J. McCarthy, *Powder Technol.*, 2001, **116**, 214–223.
25 V. Richefeu, M. S. El Youssoufi, R. Peyroux and F. Radjai, *Int. J. Numer. Anal. Methods Geomech.*, 2008, **32**, 1365–1383.
26 E. Koos, *Curr. Opin. Colloid Interface Sci.*, 2014, **19**, 575–584.
27 A. Singh, V. Magnanimo, K. Saitoh and S. Luding, *Phys. Rev. E: Stat., Nonlinear, Soft Matter Phys.*, 2014, **90**, 022202.
28 D. Faroux, K. Washino, T. Tsuji and T. Tanaka, *Phys. Rev. Fluids*, 2022, **7**, 084306.
29 H. Shi, S. Roy, T. Weinhart, V. Magnanimo and S. Luding, *Granular Matter*, 2020, **22**, 1–20.
30 Q. Luo, Q. Zheng and A. Yu, *Powder Technol.*, 2017, **314**, 121–128.
31 S. Roy, S. Luding and T. Weinhart, *EPJ Web Conf.*, 2017, **140**, 03065.
32 J. Wang, Z. Farmani, J. A. Dijksman, C. Lübeck, O. Speck and R. Stannarius, *Granular Matter*, 2022, **24**, 103.
33 D. Fenistein and M. van Hecke, *Nature*, 2003, **425**, 256.
34 D. Fenistein, J. W. van de Meent and M. van Hecke, *Phys. Rev. Lett.*, 2004, **92**, 094301.

35 Z. Farmani, N. Ghods, H. Singh, J. Wang, R. Stannarius, S. Radl, D. L. Henann and J. A. Dijksman, Pressure sensitivity in non-local flow behaviour of dense hydrogel particle suspensions, *arXiv*, 2023, preprint, arXiv:2308.00140, DOI: 10.48550/arXiv.2308.00140.
36 J. A. Dijksman and M. van Hecke, *Soft Matter*, 2010, **6**, 2901–2907.
37 T. Unger, *Phys. Rev. Lett.*, 2007, **98**, 018301.
38 M. Alam and S. Luding, *Phys. Fluids*, 2003, **15**, 2298–2312.
39 E. Kurban, D. Vescovi and D. Berzi, *Soft Matter*, 2025, **21**, 2049–2058.
40 F. Olver, D. Lozier, R. Boisvert and C. Clark, *The NIST Handbook of Mathematical Functions*, Cambridge University Press, New York, NY, 2010.
41 T. Börzsönyi, T. Unger, B. Szabó, S. Wegner, F. Angenstein and R. Stannarius, *Soft Matter*, 2011, **7**, 8330–8336.
42 J. A. Dijksman, E. Wandersman, S. Slotterback, C. R. Berardi, W. D. Updegraff, M. van Hecke and W. Losert, *Phys. Rev. E: Stat., Nonlinear, Soft Matter Phys.*, 2010, **82**, 060301.
43 Z. Farmani, J. A. Wieringa, J. van Duynhoven and J. A. Dijksman, *KONA Powder Part. J.*, 2024, 2025014.
44 R. Höhler and S. Cohen-Addad, *Soft Matter*, 2017, **13**, 1371–1383.
45 N. Brodu, J. A. Dijksman and R. P. Behringer, *Nat. Commun.*, 2015, **6**, 7361.
46 C. Shakya, L. Placidi, A. Misra, L. Kool, A. Lindner, J. Van der Gucht and J. Dijksman, 2025, DOI: 10.48550/arXiv.2506.08855.